Symmetry breaking in self-assembled M_4L_6 cage complexes

Wenjing Meng, Tanya K. Ronson, and Jonathan R. Nitschke[1]

Department of Chemistry, University of Cambridge, Cambridge CB2 1EW, United Kingdom

Edited by Francois N. Diederich, Eidgenössische Technische Hochschule Zürich, Zurich, Switzerland, and approved May 9, 2013 (received for review February 12, 2013)

Here we describe the phenomenon of symmetry breaking within a series of M_4L_6 container molecules. These containers were synthesized using planar rigid bis-bidentate ligands based on 2,6-substituted naphthalene, anthracene, or anthraquinone spacers and Fe^{II} ions. The planarity of the ligand spacer favors a stereochemical configuration in which each cage contains two metal centers of opposite handedness to the other two, which would ordinarily result in an S_4-symmetric, achiral configuration. Reduction of symmetry from S_4 to C_1 is achieved by the spatial offset between each ligand's pair of binding sites, which breaks the S_4 symmetry axis. Using larger Cd^{II} or Co^{II} ions instead of Fe^{II} resulted, in some cases, in the observation of dynamic motion of the symmetry-breaking ligands in solution. NMR spectra of these dynamic complexes thus reflected apparent S_4 symmetry owing to rapid interconversion between energetically degenerate, enantiomeric C_1-symmetric conformations.

coordination chemistry | metal–organic capsules | self-assembly | supramolecular chemistry | stereochemistry

Symmetry breaking must occur before complexity can develop (1, 2). In cosmology, the perfect symmetry of the singularity at the inception of time (3) evolved under the direction of physical laws to produce the present-day universe filled anisotropically with asymmetrical pieces of matter. In biology, a zygote must break its symmetry before the functional specialization involved with cell differentiation and tissue architecture development can occur (1, 4). Studies on model systems for biological symmetry breaking reveal that the complexity on larger scales is often underpinned by asymmetry on smaller scales (4, 5), which is a consequence of dynamic interactions at the molecular level (4). Investigations of symmetry breaking during complex molecular self-assembly phenomena thus present an opportunity to shed light upon the foundations of the evolution of matter toward complexity.

To contribute to the understanding of symmetry breaking, in the present study we demonstrate a rational method of systematic symmetry breaking within a series of M_4L_6 metal–organic tetrahedra through the control of linker geometry.

Metal–organic polyhedra (6–13) have attracted significant attention due to their host–guest behavior that can be applied in molecular storage (14–17), separation (18), and catalysis (19–22). Platonic or Archimedean metal–organic polyhedra can be constructed by a careful choice of ligands and metal ions (8, 23–27), where the geometries of the individual building blocks define the symmetry axes of the polyhedron. Although high-symmetry architectures represent a great achievement in terms of logical molecular design, lower-symmetry ones are possibly of still greater interest. Besides the fundamental interest in symmetry breaking mentioned above (1), an asymmetric capsule could achieve recognition of asymmetric substrates (28) and possibly catalyze asymmetric transformations (29). So far all reported metal–organic capsules have high symmetry (27, 30, 31), although in some cases they are chiral (29, 32–34), and specific guest molecules are observed to stabilize lower-symmetry structures (32, 35).

M_4L_6 capsules are constructed from octahedrally coordinated metal ions and linear bis-bidentate ligands. Because each vertex is defined by a metal stereocenter (Δ or Λ), an M_4L_6 structure can have T ($\Delta\Delta\Delta\Delta/\Lambda\Lambda\Lambda\Lambda$, homochiral), C_3 ($\Delta\Delta\Delta\Lambda/\Lambda\Lambda\Lambda\Delta$, heterochiral), or S_4 ($\Delta\Delta\Lambda\Lambda$, achiral) symmetry (36), with the homochiral cage being most commonly observed (33, 37–43). When the T-symmetric configuration is adopted, all metal-to-metal distances are the same, avoiding strain potentially incurred by differences in these distances present in the C_3- or S_4-symmetric configurations (44). The geometries and steric properties of the ligands can nonetheless overrule the preference for T symmetry. For example, in cages constructed from pyridyl-imine ligands via subcomponent self-assembly (45), S_4 symmetry, rather than T, was found to be the lowest-energy stereochemical configuration when the two terminal phenylene rings within the ligand spacer are forced to be coplanar (44), a configuration that is optimal for the four *syn* ligands that an S_4-symmetric cage requires to connect metal centers with opposite stereochemistry.

Building upon the S_4-symmetric framework, we hypothesized that the S_4 symmetry axis could be broken if an offset was introduced between the two coordination sites within the same ligand. We reasoned that bis(pyridylimine) ligands derived from the planar, rigid diamines **A**, **B**, or **C** (Fig. 1) could be used to introduce such an offset.

Results and Discussion

Synthesis and Characterization of Asymmetric $Fe^{II}_4L_6$ Cages. As illustrated in Fig. 1, the reactions between diamines **A**, **B**, or **C** (3 eq), 2-formylpyridine (6 eq), and either $Fe(ClO_4)_2$ or $Fe(SO_3CF_3)_2$ ($^-$OTf, 2 eq) in acetonitrile provided a new set of M_4L_6 cages as the uniquely observed products in solution, as verified by ^{1}H NMR and electrospray ionization (ESI)-MS and detailed below.

NMR spectra (Fig. 2 and *SI Appendix*, Figs. S4, S5, S7, S8, S13, S14, S17, and S18) for the corresponding products **1a**, **1b**, and **1c** (Fig. 2) contained more peaks than could be attributed to any single diastereomer of T, C_3, or S_4 symmetry, or a mixture of all three of them. Diffusion-ordered spectroscopy (DOSY) ^{1}H NMR spectra were consistent in each case with the presence of only a single species. Although there was significant peak overlap in both the ^{1}H and ^{13}C NMR spectra, it was possible to identify 12 imine carbon signals in the ^{13}C NMR and heteronuclear multiple quantum correlation spectra (HMQC), indicating the presence of 12 ligand environments with equal populations.

Author contributions: W.M. and J.R.N. designed research; W.M. performed research; W.M., T.K.R., and J.R.N. analyzed data; T.K.R. collected and analyzed the single-crystal diffraction data; and W.M., T.K.R., and J.R.N. wrote the paper.

The authors declare no conflict of interest.

This article is a PNAS Direct Submission.

Data deposition: Crystallography, atomic coordinates, and structure factors have been deposited in the Cambridge Structural Database, Cambridge Crystallographic Data Centre, Cambridge CB2 1EZ, United Kingdom (CSD reference nos. 901947–901951).

[1]To whom correspondence should be addressed. E-mail: jrn34@cam.ac.uk.

This article contains supporting information online at www.pnas.org/lookup/suppl/doi:10.1073/pnas.1302683110/-/DCSupplemental.

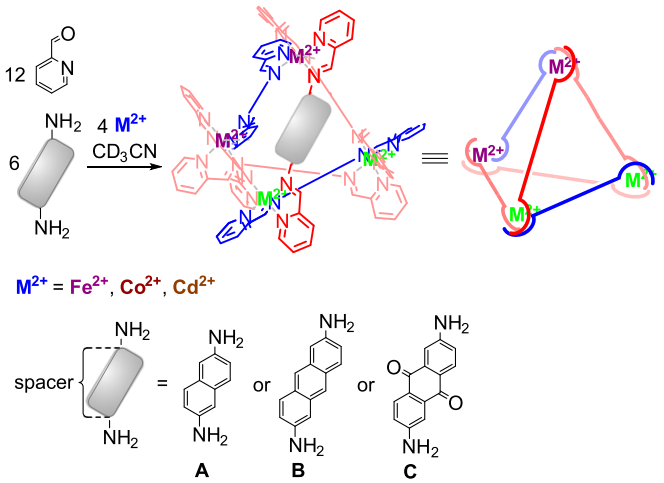

Fig. 1. Synthesis of M_4L_6 (where $L_6 = 2L_{anti} + 4L_{syn}$) structures that contain two Δ (shown in purple) and two Λ (green) metal vertices along with two *anti* and four *syn* ligands. The *anti* ligands are colored blue and the *syn* ligands red.

These observations suggest that all of the ligand hydrogen atoms are in inequivalent environments, and the cage is therefore asymmetric. A change in counter anion or in solvent (e.g., using nitromethane instead of acetonitrile) did not affect the symmetry and only resulted in slight shifts for some signals in the NMR spectra (e.g., *SI Appendix*, Figs. S4 and S7).

Vapor diffusion of diisopropyl ether into a nitromethane solution of cage **1a**·ClO_4 allowed the isolation of single crystals suitable for X-ray analysis. The crystal structure (Fig. 3) confirmed the presence of the M_4L_6 cage framework. The unit cell contains two cages that are enantiomers of each other. The cage is crystallographically asymmetric yet has many features in common with an S_4-symmetric framework: Two Fe^{II} centers are of the same handedness whereas the other two are of the opposite handedness; each pair of Fe^{II} centers of the same stereochemistry is connected by ligands adopting *anti* conformations, whereas the other four ligands are *syn*.

The offset geometry of the naphthyl spacers causes them to adopt an arrangement whereby within each ligand one ring is oriented inward, roughly toward the center of the cage and one ring points outward. As shown in Fig. 3, an S_4 operation (consisting of a 90° rotation about the axis that bisects both *anti* ligands of **1a**, followed by a reflection through a mirror plane perpendicular to this axis) results in a configuration in which all *syn* ligands are indistinguishable from their arrangement before the operation, but where the *anti* ligands have adopted a different arrangement. These two configurations are enantiomeric mirror images of each other. If the naphthyl groups of the *anti* ligands were to adopt a conformation twisted by 90° in either direction along their N-N axes (i.e., where the ligand becomes planar), the S_4 operation would result in a configuration indistinguishable from the initial one, and the molecule would possess S_4 symmetry. Models suggest (*SI Appendix*, Fig. S37), however, that such an S_4-symmetric configuration would result in steric clashes between naphthyl rings.

The asymmetric configurations assumed by the ligands thus allow the naphthyl rings to avoid steric clashes with each other near the metal centers, reducing strain. The ligands pack tightly together (*SI Appendix*, Fig. S33), which eliminates any cavity space and provides additional stabilizing CH–π interactions between neighboring naphthalene rings.

Fe–Fe distances in **1a** are in the range of 10.368(4)–10.724(4) Å; the two Fe^{II} centers linked by an *anti* ligand are 0.3 Å farther away from each other than those connected by a *syn* ligand. The Fe^{II}–N bond lengths are in the range of 1.96–2.01 Å, consistent with the low-spin configuration observed by NMR.

Either of the enantiotopic conformations of the *anti* ligands of **1a** (Fig. 3) could be adopted with minimal energetic perturbation to the overall cage framework, as highlighted by disorder observed in the X-ray structures of both the perchlorate and the trifluoromethanesulfonate salts of **1a**. Whereas the *syn* ligands in this structure (and all others reported herein) were observed to be well-ordered, the naphthyl groups of one (in **1a**·ClO_4) or both (in **1a**·OTf; *SI Appendix*, Fig. S34) of the *anti* ligands were observed to be disordered across two positions.

X-ray–quality crystals of anthracene-edged cage **1b**·OTf were obtained by vapor diffusion of diethyl ether into an acetonitrile solution of the cage. Cage **1b**·OTf is also asymmetric in the solid state with no disorder observed (Fig. 4). The Fe–Fe distances are 12.131(3)–12.894(4) Å, a range of variation 0.3 Å wider than the naphthalene-edged cage **1a**·ClO_4. The longer edges also engender a discrete void space within cage **1b**, whereas **1a** showed no internal void. The VOIDOO program revealed the shape of this 16.8 $Å^3$ cavity (Fig. 4), showing how the C_1 symmetry of host **1b** is imposed on the shape of its cavity. The small cavity size is attributed to the packing of the anthracene spacers to minimize steric clashes, as with **1a**.

The ^1H NMR spectra of dissolved crystals of **1a** (i.e., both **1a**·ClO_4 and **1a**·OTf) and **1b** were indistinguishable from that of the corresponding cage freshly prepared from subcomponents in acetonitrile, indicating the rotation of the *anti* ligands about their N-N axes is slow on the NMR time scale, and therefore C_1 symmetry is the lowest energy configuration for the system in solution. For all of the three Fe^{II} cages **1a**, **1b**, and **1c**, when the temperature was increased to 343 K (*SI Appendix*, Figs. S12, S16, and S20), neither decomposition nor coalescence was observed in the ^1H NMR spectrum, indicating relatively high thermal stability of the complexes and limited rotational freedom of the ligands.

$Co^{II}_4L_6$ and $Cd^{II}_4L_6$ Cages. $Co(BF_4)_2$ (4 eq) was also observed to form M_4L_6 structures with both diamines **A** and **B** (6 eq) and 2-formylpyridine (12 eq); when **C** was used an insoluble product was obtained. These products, **2a** and **2b**, were characterized in solution by paramagnetic ^1H NMR spectroscopy and ESI-MS. In similar fashion to the Fe^{II} cage **1a**, Co^{II} cage **2a** also exhibited 12 imine signals in the ^1H NMR spectrum (*SI Appendix*, Fig. S21), indicating that cage **2a** is also asymmetrical.

The crystal structure obtained for **2a**·BF_4 (*SI Appendix*, Fig. S35) shows the same overall configuration as the iron analog **1a**. The coordination bond lengths are in the range of 2.117(6)–2.197(6) Å, on average 0.15 Å longer than that for Fe–N in **1a**·ClO_4. The average bond length for Co–N_{imine} is around 0.03 Å longer than that for Co–N_{py}, and no significant Jahn–Teller distortion was observed, consistent with the presence of Co^{II} ions

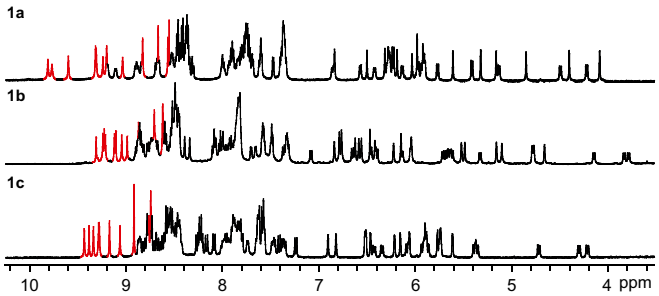

Fig. 2. The ^1H NMR spectra for $Fe^{II}_4L_6$ cages **1a**·OTf, **1b**·OTf, **1c**·OTf, with imine protons in red.

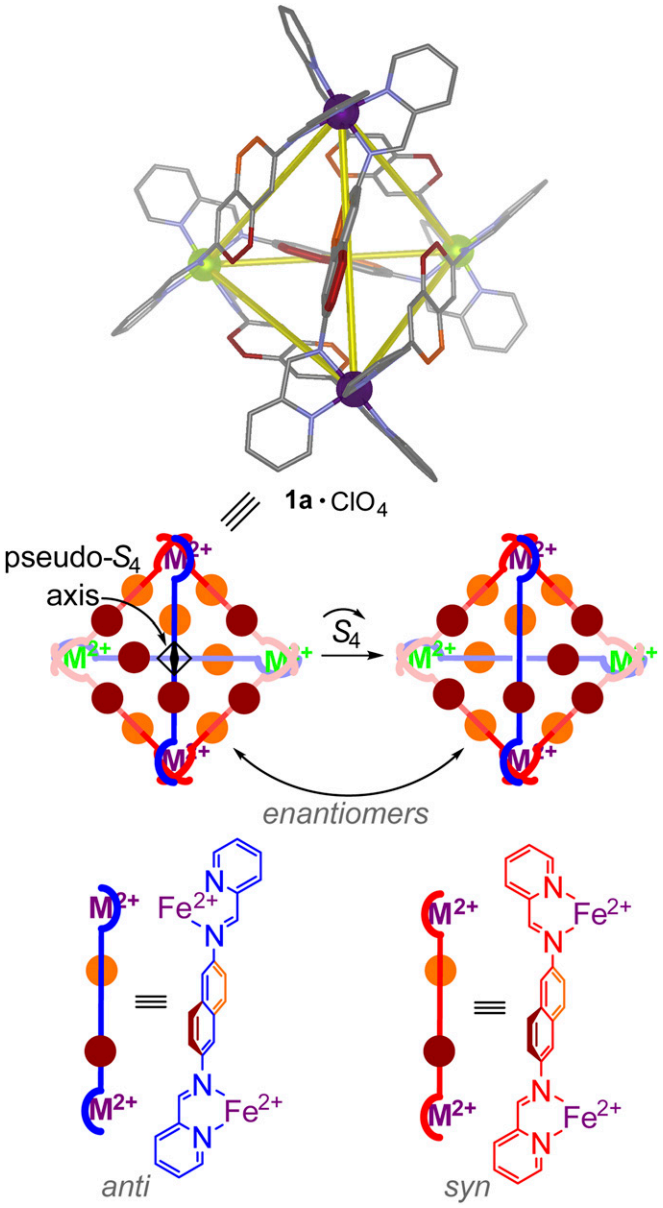

Fig. 3. (*Upper*) Crystal structure of Fe^{II} cage **1a**·ClO_4 (counter anions, solvent molecules and hydrogen atoms are omitted for clarity; only one conformation of the disordered naphthyl group is shown). (*Lower*) A schematic illustration of how the S_4 axis of symmetry is broken. The Δ and Λ metal centers are colored purple and green, respectively. The *anti* ligands are colored blue and the *syn* ligands red. The parts of the naphthyl spacer that point out of and into the plane of the page are colored orange and maroon, respectively.

in the high-spin state. There is a wider range of Co–Co distances in **2a**·BF_4 [10.339(3)–10.947(5) Å] compared with the Fe–Fe distances in **1a** and correspondingly greater distortions from idealized octahedral geometry in the Co^{II} cage.

Intriguingly, the analogous tetrahedron **2b**·BF_4 has a much simpler ^{1}H NMR spectral profile (*SI Appendix*, Fig. S25). Only three imine signals were observed, consistent with S_4 symmetry on the NMR time scale. We infer that the anthracenyl groups of the *anti* ligands of **2b** were undergoing rapid rotation, as opposed to adopting an S_4-symmetric lowest-energy state, based upon our observations of their analogs and examination of models, which suggested that for Co^{II}, as for Cd^{II} and Fe^{II}, the S_4-symmetric configuration would experience steric clashes (*SI Appendix*, Fig. S37).

The ^{1}H NMR peaks for **2b**·BF_4 were observed to sharpen as the temperature increased, indicating fast thermal motion within the complex; these peaks broadened into the baseline below 15 °C, consistent with a slowing of the *anti* ligands' rotation about their N-N axes below this temperature (*SI Appendix*, Fig. S26). No coalescence of the ^{1}H NMR signals of **2a**·BF_4 was observed upon increasing the temperature to 70 °C (*SI Appendix*, Fig. S23), indicating that the *anti* ligands do not rotate about their N-N axes at a rate comparable to the NMR time scale at this temperature. We attribute the faster ligand rotation in **2b** than in **2a** to the looser geometrical requirements imposed by the longer Co–N bonds, which allow the individual ligands to rotate past each other with a lower energetic penalty and to the greater lability of these bonds, which may loosen along one N–Co–N axis by undergoing Jahn–Teller distortion during ligand rotation.

Cd^{II} was not observed to template the formation of a single product with **B** or **C** under the conditions that gave clean cage formation with Fe^{II}; instead, mixtures of soluble and insoluble products were obtained. Cage **3a** was generated cleanly, however, when diamine **A** was used, as confirmed by its ^{1}H NMR spectrum (*SI Appendix*, Fig. S27). NMR spectra of **3a** were consistent with rapid rotation of the *anti* ligands even at −35 °C in solution (*SI Appendix*, Fig. S32), in contrast to its Fe^{II} or Co^{II} analogs. As with **2b**, we infer **3a** to undergo interconversion between enantiomeric C_1-symmetric configurations rapidly on the NMR time scale, such as to exhibit apparent S_4 symmetry, as opposed to adopting an S_4-symmetric lowest-energy state. We hypothesize that steric clashes between ligands during these interconversions would incur a lower energetic penalty owing to the larger ionic radius of Cd^{II}, resulting in the more rapid rate of rotation observed in the case of this metal ion. We infer that the mechanism of ligand rotation may involve distortion of the

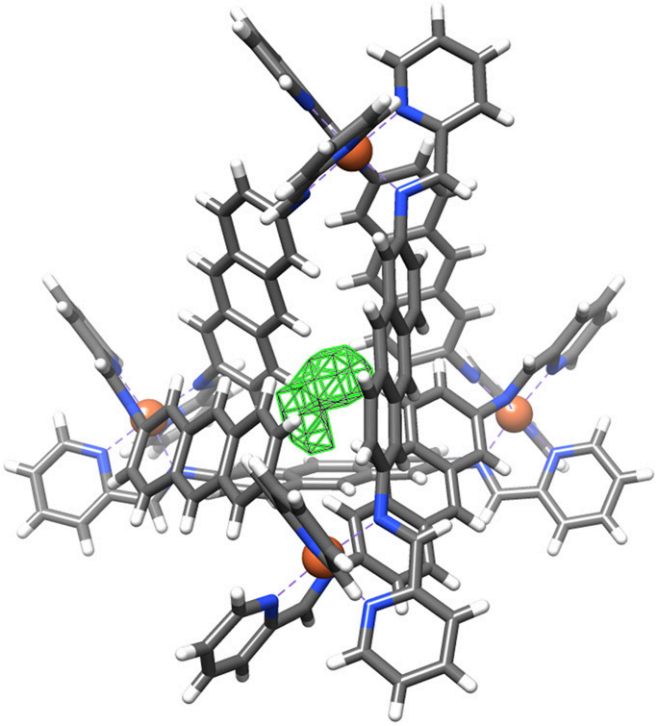

Fig. 4. The X-ray crystal structure of cage **1b**, superimposed upon a plot of the asymmetric cavity (16.8 $Å^3$) found with VOIDOO (46).

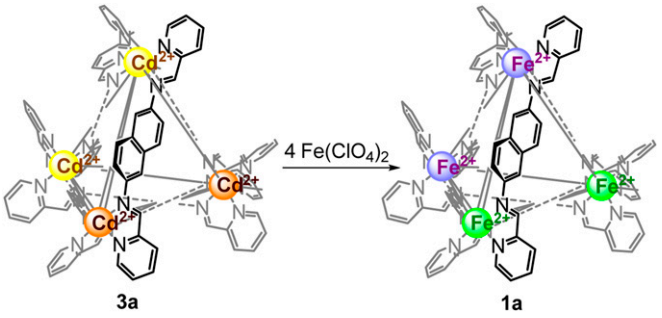

Fig. 5. Transformation of **1c**·ClO_4 into **1a**·ClO_4 via metal exchange.

coordination sphere of Cd^{II}, but not breaking of the Cd–N_{imine} linkage on the NMR time scale, because satellite peaks were associated with the imine ^{1}H NMR resonances of **3a**, attributable to *J*-coupling with the two spin-1/2 isotopes of cadmium (*SI Appendix*, Fig. S27).

Because Cd^{II} has a d^{10} electron configuration, cage **3a** does not benefit from crystal field stabilization, and its metal–ligand bonds are thus weaker than in complex **1a**. When $Fe(ClO_4)_2$ (4 eq per cage) was added to an acetonitrile solution of cage **3a**·ClO_4, the orange solution turned dark purple immediately, suggesting rapid formation of a Fe^{II} complex. Cage **1a**·ClO_4 was the only observed complex in both the ^{1}H NMR spectrum (*SI Appendix*, Fig. S36) and ESI-MS of the reaction mixture, with no evidence for the presence of **3a** or any mixed-metal species, consistent with a clean metal displacement where Fe^{II} substituted all Cd^{II} to transform cage **3a**·ClO_4 into cage **1a**·ClO_4 (Fig. 5), halting the *anti* ligands' rapid rotation. Although transmetallation has been demonstrated in macrocyclic complexes (47) and helicates (48), to our knowledge this is a unique example of the conversion of one metal–organic polyhedron into another via metal exchange.

Conclusions

We have demonstrated that by introducing an offset between the two metal binding sites within a linear bis-bidentate ligand an asymmetric M_4L_6 cage structure could be generated. This symmetry breaking was achieved as a consequence of three features of the system. First, this class of cages (44) is known, when both ends of the diamine spacer are forced to be coplanar, to adopt a configuration where two metal centers have the opposite handedness to the other two, resulting ordinarily in an S_4-symmetric structure. Second, the diamine spacer's offset geometry breaks the erstwhile S_4 symmetry axis, due to steric interactions between the naphthyl groups. Third, racemization of these asymmetric cages, via rotation of the spacer groups of the *anti* ligands, can be slowed through the use of Fe^{II} as the metal ion. The shorter Fe^{II}–N bonds led to higher energetic barriers to ligand torsion, locking the cage's stereochemistry.

The phenomenon of asymmetric cage formation was observed to be general across three metal ions and three offset spacer groups; other metal ions and spacers also thus show promise because the steric effects giving rise to symmetry breaking operate next to the metal centers (*SI Appendix*, Fig. S37), independently of ligand length. Although the cavity of the largest cage structurally characterized herein, **1b** (Fig. 4), is too small for even the smallest chiral guest, the methods outlined here demonstrate how larger asymmetrical cages, imprinted with stereochemical information (29, 32–34), might selectively encapsulate and asymmetrically transform low-symmetry, information-rich guest species.

Materials and Methods

Syntheses and characterization (i.e., ^{1}H NMR, ^{13}C NMR, mass spectra, elemental analysis, and crystallography) of all new compounds are described in the text of *SI Appendix*. Details of experimental instrumentation are summarized in the text of *SI Appendix*. Further discussion on the mechanism of symmetry breaking is available in *SI Appendix*.

ACKNOWLEDGMENTS. We thank the NMR service team at the Cambridge Chemistry Department for carrying out some of the NMR spectroscopy and Diamond Light Source (United Kingdom) for synchrotron beam time on I19 (MT7114 and MT7569). This work was supported by the European Research Council.

1. Anderson PW (1972) More is different. *Science* 177(4047):393–396.
2. Livio M (2012) Physics: Why symmetry matters. *Nature* 490(7421):472–473.
3. Lemaître G (1927) Un Univers homogène de masse constante et de rayon croissant rendant compte de la vitesse radiale des nébuleuses extra-galactiques. *Ann. Soc. Sci. Brux. A* 47:49–59.
4. Li R, Bowerman B (2010) Symmetry breaking in biology. *Cold Spring Harb Perspect Biol* 2(3):a003475.
5. Mullins RD (2010) Cytoskeletal mechanisms for breaking cellular symmetry. *Cold Spring Harb Perspect Biol* 2(1):a003392.
6. Ward MD (2009) Polynuclear coordination cages. *Chem Commun (Camb)* (30): 4487–4499.
7. Dalgarno SJ, Power NP, Atwood JL (2008) Metallo-supramolecular capsules. *Coord Chem Rev* 252(8-9):825–841.
8. Fujita M, Tominaga M, Hori A, Therrien B (2005) Coordination assemblies from a Pd(II)-cornered square complex. *Acc Chem Res* 38(4):369–378.
9. Saalfrank RW, Maid H, Scheurer A (2008) Supramolecular coordination chemistry: The synergistic effect of serendipity and rational design. *Angew Chem Int Ed Engl* 47(46): 8794–8824.
10. Tranchemontagne DJ, Ni Z, O'Keeffe M, Yaghi OM (2008) Reticular chemistry of metal-organic polyhedra. *Angew Chem Int Ed Engl* 47(28):5136–5147.
11. Seidel SR, Stang PJ (2002) High-symmetry coordination cages via self-assembly. *Acc Chem Res* 35(11):972–983.
12. Ghosh K, Hu J, White HS, Stang PJ (2009) Construction of multifunctional cuboctahedra via coordination-driven self-assembly. *J Am Chem Soc* 131(19): 6695–6697.
13. Zheng Y-R, et al. (2010) Coordination-driven self-assembly of truncated tetrahedra capable of encapsulating 1,3,5-triphenylbenzene. *Inorg Chem* 49(22):10238–10240.
14. Dong VM, Fiedler D, Carl B, Bergman RG, Raymond KN (2006) Molecular recognition and stabilization of iminium ions in water. *J Am Chem Soc* 128(45):14464–14465.
15. Mal P, Breiner B, Rissanen K, Nitschke JR (2009) White phosphorus is air-stable within a self-assembled tetrahedral capsule. *Science* 324(5935):1697–1699.
16. Sawada T, Yoshizawa M, Sato S, Fujita M (2009) Minimal nucleotide duplex formation in water through enclathration in self-assembled hosts. *Nat Chem* 1(1):53–56.
17. Yoshizawa M, Tamura M, Fujita M (2007) Chirality enrichment through the heterorecognition of enantiomers in an achiral coordination host. *Angew Chem Int Ed Engl* 46(21):3874–3876.
18. Riddell IA, Smulders MMJ, Clegg JK, Nitschke JR (2011) Encapsulation, storage and controlled release of sulfur hexafluoride from a metal-organic capsule. *Chem Commun (Camb)* 47(1):457–459.
19. Yoshizawa M, Tamura M, Fujita M (2006) Diels-alder in aqueous molecular hosts: unusual regioselectivity and efficient catalysis. *Science* 312(5771):251–254.
20. Pluth MD, Bergman RG, Raymond KN (2007) Acid catalysis in basic solution: a supramolecular host promotes orthoformate hydrolysis. *Science* 316(5821):85–88.
21. Hastings CJ, Fiedler D, Bergman RG, Raymond KN (2008) Aza Cope rearrangement of propargyl enammonium cations catalyzed by a self-assembled "nanozyme." *J Am Chem Soc* 130(33):10977–10983.
22. Kuil M, Soltner T, van Leeuwen PWNM, Reek JNH (2006) High-precision catalysts: regioselective hydroformylation of internal alkenes by encapsulated rhodium complexes. *J Am Chem Soc* 128(35):11344–11345.
23. Albrecht M, Janser I, Frohlich R (2005) Catechol imine ligands: From helicates to supramolecular tetrahedra. *Chem Commun (Camb)* (2):157–165.
24. Caulder DL, Raymond KN (1999) Supermolecules by design. *Acc Chem Res* 32(11): 975–982.
25. Liu Y, et al. (2004) Directed assembly of metal-organic cubes from deliberately predesigned molecular building blocks. *Chem Commun (Camb)* (24):2806–2807.
26. Sun Q-F, Sato S, Fujita M (2012) An $M_{18}L_{24}$ stellated cuboctahedron through post-stellation of an $M_{12}L_{24}$ core. *Nat Chem* 4(4):330–333.
27. Meng W, et al. (2011) A self-assembled M_8L_6 cubic cage that selectively encapsulates large aromatic guests. *Angew Chem Int Ed Engl* 50(15):3479–3483.
28. Fiedler D, Leung DH, Bergman RG, Raymond KN (2005) Selective molecular recognition, C-H bond activation, and catalysis in nanoscale reaction vessels. *Acc Chem Res* 38(4):349–358.
29. Lee SJ, Hu A, Lin W (2002) The first chiral organometallic triangle for asymmetric catalysis. *J Am Chem Soc* 124(44):12948–12949.
30. Olenyuk B, Levin MD, Whiteford JA, Shield JE, Stang PJ (1999) Self-assembly of nanoscopic dodecahedra from 50 predesigned components. *J Am Chem Soc* 121(44): 10434–10435.

31. Tominaga M, et al. (2004) Finite, spherical coordination networks that self-organize from 36 small components. *Angew Chem Int Ed Engl* 43(42):5621–5625.
32. Ziegler M, Davis AV, Johnson DW, Raymond KN (2003) Supramolecular chirality: A reporter of structural memory. *Angew Chem Int Ed Engl* 42(6):665–668.
33. Argent SP, Riis-Johannessen T, Jeffery JC, Harding LP, Ward MD (2005) Diastereoselective formation and optical activity of an M_4L_6 cage complex. *Chem Commun (Camb)* (37):4647–4649.
34. Ousaka N, Clegg JK, Nitschke JR (2012) Nonlinear enhancement of chiroptical response through subcomponent substitution in M_4L_6 cages. *Angew Chem Int Ed Engl* 51(6):1464–1468.
35. Jiang W, Rebek J, Jr. (2012) Guest-induced, selective formation of isomeric capsules with imperfect walls. *J Am Chem Soc* 134(42):17498–17501.
36. Beissel T, Powers RE, Parac TN, Raymond KN (1999) Dynamic isomerization of a supramolecular tetrahedral M_4L_6 cluster. *J Am Chem Soc* 121(17):4200–4206.
37. Stang PJ, Olenyuk B, Muddiman DC, Smith RD (1997) Transition-metal-mediated rational design and self-assembly of chiral, nanoscale supramolecular polyhedra with unique T symmetry. *Organometallics* 16(14):3094–3096.
38. Mal P, Schultz D, Beyeh K, Rissanen K, Nitschke JR (2008) An unlockable-relockable iron cage by subcomponent self-assembly. *Angew Chem Int Ed Engl* 47(43): 8297–8301.
39. Caulder DL, Powers RE, Parac TN, Raymond KN (1998) The self-assembly of a predesigned tetrahedral M_4L_6 supramolecular cluster. *Angew Chem Int Ed Engl* 37(13-14): 1840–1843.
40. Tidmarsh IS, et al. (2009) Further investigations into tetrahedral M_4L_6 cage complexes containing guest anions: New structures and NMR spectroscopic studies. *New J Chem* 33(2):366–375.
41. Albrecht M, Burk S, Weis P (2008) Chiral confined space: Induction of stereochemistry in a M_4L_4 metallosupramolecular container. *Synthesis* (18):2963–2967.
42. Saalfrank RW, et al. (2002) Enantiomerisation of tetrahedral homochiral $[M_4L_6]$ clusters: Synchronised four Bailar twists and six atropenantiomerisation processes monitored by temperature-dependent dynamic 1H NMR spectroscopy. *Chemistry* 8(12):2679–2683.
43. Cotton FA, Murillo CA, Yu R (2005) Deliberate synthesis of the preselected enantiomer of an enantiorigid molecule with pure rotational symmetry T. *Dalton Trans* (19): 3161–3165.
44. Meng W, Clegg JK, Thoburn JD, Nitschke JR (2011) Controlling the transmission of stereochemical information through space in terphenyl-edged Fe_4L_6 cages. *J Am Chem Soc* 133(34):13652–13660.
45. Nitschke J, Ronson T, Zarra S, Black SP (2012) Metal-organic container molecules through subcomponent self-assembly. *Chem Commun (Camb)* (49):2476–2490.
46. Kleywegt GJ, Jones TA (1994) Detection, delineation, measurement and display of cavities in macromolecular structures. *Acta Crystallogr D Biol Crystallogr* 50(Pt 2): 178–185.
47. Beckmann U, et al. (2003) Dicobalt(II) complexes of a triazolate-containing Schiff-base macrocycle: Synthesis, structure and magnetism. *Dalton Trans* (7):1308–1313.
48. Dömer J, Slootweg JC, Hupka F, Lammertsma K, Hahn FE (2010) Subcomponent assembly and transmetalation of dinuclear helicates. *Angew Chem Int Ed Engl* 49(36): 6430–6433.